Vortex-induced vibration of a flexible pipe under oscillatory sheared flow

Xuepeng Fu, Shixiao Fu,* Mengmeng Zhang, Haojie Ren, Bing Zhao, and Yuwang Xu
State Key Laboratory of Ocean Engineering, Shanghai Jiao Tong University, Shanghai 200240, China and Institute of Polar and Ocean Technology, Institute of Marine Equipment, Shanghai Jiao Tong University, Shanghai 200240, China

(Received 24 May 2023; accepted 14 December 2023; published 25 January 2024)

A vortex-induced vibration (VIV) test of a tensioned flexible pipe in oscillatory sheared flow was performed in an ocean basin. The model was 28.41 mm in diameter and 3.88 m in length. The test was performed on a rotating test rig to simulate oscillatory sheared flow conditions. One end of the test pipe is fixed, and one end is forced to harmonically oscillate to simulate oscillatory sheared flows with various combinations of amplitudes and periods, Keulegan-Carpenter (KC) numbers from 25 to 160, and five kinds of reduced velocities V_r from 6 to 14. Fiber Bragg grating strain sensors were arranged along the test pipe to measure bending strains, and the modal analysis approach was used to determine the VIV response. The VIV response in the cross-flow direction is investigated. The results show that VIV under oscillatory sheared flow exhibits amplitude modulation and hysteresis phenomena. Compared with oscillatory uniform flow-induced VIV, the Strouhal number is smaller in oscillatory sheared flow-induced VIVs. The VIV developing process in oscillatory sheared flow is analyzed, and critical KC is proposed to describe the occurrence of modulated VIV under oscillatory sheared flow.

DOI: 10.1103/PhysRevFluids.9.014604

I. INTRODUCTION

Vortex-induced vibration (VIV) is a phenomenon that has been extensively studied over the past few decades due to its significant impact on the fatigue damage and drag forces of slender structures such as risers and tension legs in offshore engineering structures. VIV occurs when fluid flows past these structures, creating a vortex street that induces mechanical oscillations in the in-line (IL) and cross-flow (CF) directions. VIV can lead to fatigue damage and ultimately structural failure if not properly accounted for in the design and operation of these structures. A series of studies for VIV have been conducted and can be found in [1–7].

Previous studies of VIV have focused primarily on the VIV response of flexible structures under steady flow fields, such as uniform flow [8], linearly sheared flow [9], stepped flow [10], and inclined uniform flow [11]. One of the detailed studies regarding the VIV flexible pipes is the Norwegian Deepwater Program (NDP) joint industrial project. NDP [12] has performed a series of VIV experiments on flexible risers in uniform flow and linearly sheared flow. Many empirical prediction models have been proposed and revised based on experimental results, such as SHEAR7 [13], VIVANA [14], and VIVA [15].

However, flexible slender structures in actual ocean engineering always suffer from spatiotemporally varying flow fields. Wang *et al.* [16] conducted a VIV experiment of a steel catenary riser (SCR) under a vessel motion-induced complex flow field. Wang *et al.* [17] simplified such a complex spatiotemporally varying flow field to oscillatory uniform flow and investigated the VIV

*shixiao.fu@sjtu.edu.cn

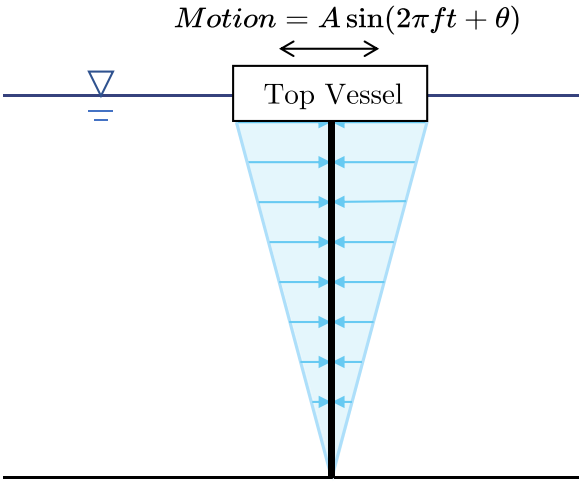

FIG. 1. Sketch of the top vessel motion-induced oscillatory sheared flow. The top vessel motion is assumed to be a harmonic motion.

characteristics of flexible cylinders under oscillatory uniform flow [18]. However, to the best of our knowledge, there have been no VIV experiments on slender pipes in oscillatory sheared flow.

Oscillatory sheared flow is an important flow field to consider when designing and operating offshore structures. Top tension risers (TTRs), for example, are often used to connect a floating production platform to the seabed. One end of the TTR is fixed to the platform, while the other end is forced to move with the top vessel motion, which generates an oscillatory sheared flow, as shown in Fig. 1. This flow field can significantly impact the VIV response of the TTR, but little is currently known regarding the VIV characteristics of slender pipes in oscillatory sheared flow.

In the present study, we aim to fill this gap in knowledge by performing an VIV experiment of a flexible pipe in oscillatory sheared flow. The model used in this study has a diameter of 28.41 mm and a length of 137 diameters. This study will provide important insights and benchmark data into the VIV characteristics of slender pipes in oscillatory sheared flow and help to improve the design and operation of offshore structures.

II. EXPERIMENTAL SETUP

A. Test apparatus

The model test was performed in the ocean basin of the State Key Laboratory of Ocean Engineering at Shanghai Jiao Tong University. The experimental apparatus, which includes the rotating rig and the tested pipe model, is installed on the false bottom of the basin, as shown in Fig. 2. The experimental apparatus produced the flow field by rotating through a timing belt motivated by the servo motor. This novel VIV experimental apparatus has been validated through credibility analysis, including noise signal analysis, repetitive experiments, and water depth tests, as shown in previously published research [19,20]. In contrast to the experiment of VIV under bidirectionally sheared flow, we set a fixing device in the center of the test apparatus. The test pipe model was installed on two sides of the edge of the test apparatus (driven wheel) and fixing device, which was equipped with clamps, U joints, and a force sensor. A pretension force of 550 N was applied to the pipe model through the tensioner.

The coordinate system was defined as *O-XYZ*, as shown in Fig. 2. The origin (*O*) was set at one ending point of the pipe model connected with a fixing device. The *X*, *Y,* and *Z* axes were along the IL, CF, and axis of the test pipe model. The rotation direction during the experiment was always along the *X* axis, and the effective current profile is shown with colors and arrows.

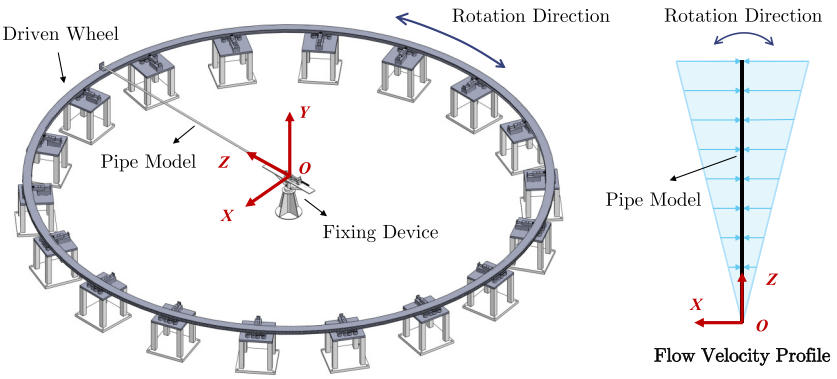

FIG. 2. Sketch of the experimental apparatus. Left: experimental apparatus with a rotating wheel driven by a servo motor; Right: effective flow velocity profile.

The primary physical properties of the test pipe model are listed in Table I. The first natural frequencies were obtained by a free decay experiment, and the calculated first natural frequency in water was calculated by Fig. 1. The theoretical value of the first natural frequency differed from the experimentally measured value by 5%:

$$f_{cn} = \frac{n^2\pi}{2}\sqrt{\left(1 + \frac{L^2 T_0}{n^2\pi^2 EI}\right)\frac{EI}{\bar{m}' L^4}}, \quad \bar{m}' = \bar{m} + \frac{1}{4}C_m \rho \pi D^2 (C_m = 1.00) \quad (n = 1, 2, 3, \ldots), \quad (1)$$

where T_0 is the pretension, and $\bar{m}$ and $\bar{m}'$ are the mass per unit length in air and still water, respectively. D, L, and EI are the diameter, length, and bending stiffness of the test pipe model, respectively. ρ is the density of water, $\rho = 1000$ kg/m^3, and the added mass coefficient C_m was set to 1.00 [21]. The mass ratio is designed based on a real steel catenary riser, and the tension is given to ensure the pipe model is tension dominated.

A total of 24 fiber Bragg grating (FBG) strain sensors in four groups are installed along the test pipe to measure dynamic strains in both the IL and CF directions, as shown in Fig. 3. There are five strain gauge points distributed in the CF direction and seven strain gauge points distributed in the IL direction. The strains along the pipe model were synchronously recorded at a sampling frequency of 250 Hz.

TABLE I. Physical properties of the test pipe model.

Parameter	Value of test model
Pipe model length L [m]	3.88
Outer diameter D [mm]	28.41
Mass in air $\bar{m}$ [kg/m]	1.24
Pretension T_0 [N]	490
Bending stiffness EI [Nm^2]	58.6
Tensile stiffness EA [N]	9.4×10^5
Damping ratio ζ [%]	2.58
Mass ratio m^*	1.96
Tested first natural frequency in water f_{n1} [Hz]	2.29
Calculated first natural frequency in water f_{cn1} [Hz]	2.20

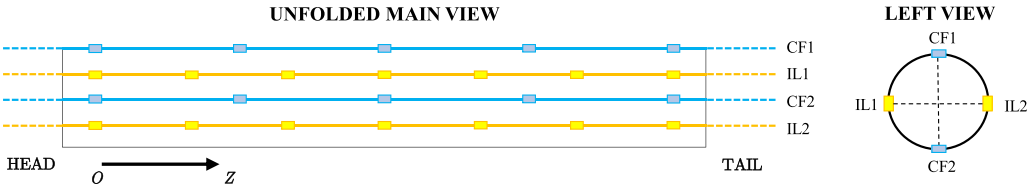

FIG. 3. Locations of the FBG strain sensors along the test pipe model.

B. Test condition

The pipe model is forced to perform oscillatory motion during the experiment to simulate the oscillatory sheared flow. In contrast to the oscillatory uniform flow test, the motion along the pipe model is varied in the present study. We define the motion of the endpoint ($Z = L$) with the maximum flow velocity as

$$X_m(t) = A_m \sin(2\pi f_o t), \tag{2}$$

$$U_m(t) = \dot{X}_m(t) = 2\pi f_0 A_m \sin(2\pi f_o t), \tag{3}$$

where $X_m(t)$ is the motion of the endpoint, $U_m(t)$ is the velocity of the forced motion, A_m is the oscillation amplitude, and f_o is the oscillation frequency. The oscillation period T is defined as $1/f_o$. The Keulegan-Carpenter number (KC), reduced velocity (V_r), and maximum Reynolds number ($\mathrm{Re_{max}}$) are used in the present study and defined as

$$\mathrm{KC} = \frac{2\pi A_m}{D}, \tag{4}$$

$$V_r = \frac{2\pi f_o A_m}{f_{cn1} D}, \tag{5}$$

$$\mathrm{Re_{max}} = \frac{U_{\max}}{\nu D}, \tag{6}$$

where f_{cn1} is the calculated first natural frequency, as shown in Table I, $\nu = 1.00 \times 10^{-6}$ is the kinematic viscosity of fluid. Five kinds of reduced velocities $V_r = 6, 8, 10, 12$, and 14 with KC varying from 20 to 160 are carried out. The corresponding maximum Reynolds number ($\mathrm{Re_{max}}$) are 10 654, 14 205, 17 757, 21 308, and 24 860, respectively.

III. DATA ANALYSIS

A. Preprocessing

The measured strain at the sensor location in the CF direction $\varepsilon_{CF}(z,t)$ contains two parts: the variable axial strain $\varepsilon_T(t)$ caused by varying tension, and the bending strain $\varepsilon_{VIV}(z,t)$ caused by VIV. The strain at z locations of CF1 and CF2 can therefore be written as

$$\varepsilon_{CF1}(z,t) = \varepsilon_T(t) + \varepsilon_{CF-VIV}(z,t), \tag{7}$$

$$\varepsilon_{CF2}(z,t) = \varepsilon_T(t) - \varepsilon_{CF-VIV}(z,t). \tag{8}$$

Combining Eqs. (7) and (8), the CF VIV strain at the z location can be calculated by

$$\varepsilon_{CF-VIV}(z,t) = [\varepsilon_{CF1}(z,t) - \varepsilon_{CF2}(z,t)]/2. \tag{9}$$

Since the VIV in the IL direction is a periodic process with a mean value of zero, the time-averaged value of the IL-VIV strain equals zero:

$$\overline{\varepsilon_{IL-VIV}(z,t)} = 0. \tag{10}$$

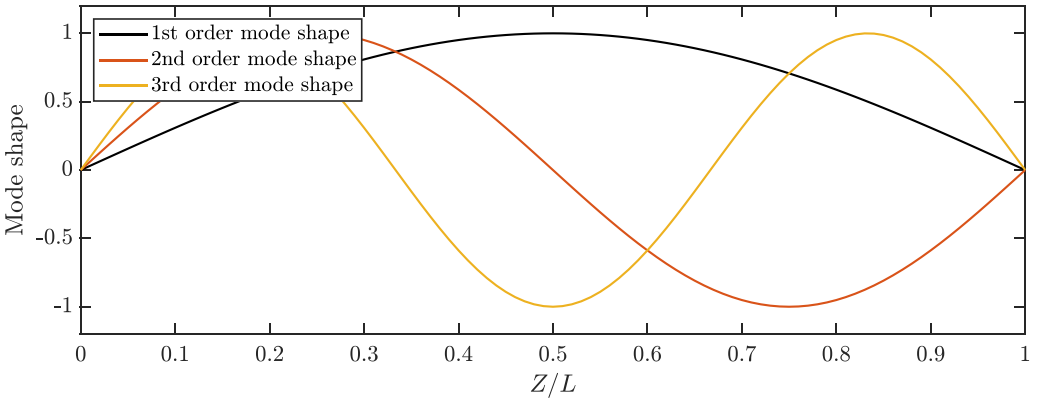

FIG. 4. First three vibration mode $\varphi(z)$ of the pipe model.

The IL VIV strain can be derived as

$$\varepsilon_{\text{initial}}(z) = \left[\overline{\varepsilon_{IL1}(z,t)} - \overline{\varepsilon_{IL2}(z,t)}\right]/2, \tag{11}$$

$$\varepsilon_{IL-VIV}(z,t) = \left[\varepsilon_{IL1}(z,t) - \varepsilon_{IL2}(z,t) - \overline{\varepsilon_{IL1}(z,t)} + \overline{\varepsilon_{IL2}(z,t)}\right]/2. \tag{12}$$

Bandpass filtering was applied to the strain signal to eliminate unavoidable noise [22]. The high-pass and low-pass cutoffs were 0.8 Hz and 20 Hz, respectively.

B. Modal analysis method

The VIV displacement in the IL and CF directions can be obtained by the modal analysis method through the measured IL and CF VIV strain.

The modal analysis method assumes that the VIV displacement can be expressed as a sum of the modal shapes multiplied by the modal weights at each time step. The VIV displacement in the CF direction can be expressed as

$$y(z,t) = \sum_{i=1}^{n} p_i(t)\varphi_i(z), \quad z \in [0, L], \tag{13}$$

where $y(z,t)$ is the VIV displacement in the CF direction at the z location, $p_i(t)$ is the ith modal weight of the displacement at time t, and $\varphi_i(z)$ is the ith modal shape of the displacement at the z location. Figure 4 displays the first three modes of the pipe model.

Based on the small deformation assumption, the curvature $\kappa(z,t)$ can be derived from the displacement modal shape as

$$\kappa(z,t) = \frac{\partial^2 y(z,t)}{\partial z^2} = \sum_{i=1}^{n} p_i(t)\varphi_i''(z), \quad z \in [0, L], \tag{14}$$

where $\varphi''(z)$ is the ith modal weight of the curvature. Based on the relationship between curvature and strain, we have

$$\varepsilon(z,t) = \kappa(z,t)R = R\sum_{i=1}^{n} p_i(t)\varphi_i''(z), \quad z \in [0, L], \tag{15}$$

where $R = D/2$ is the radius of the pipe model.

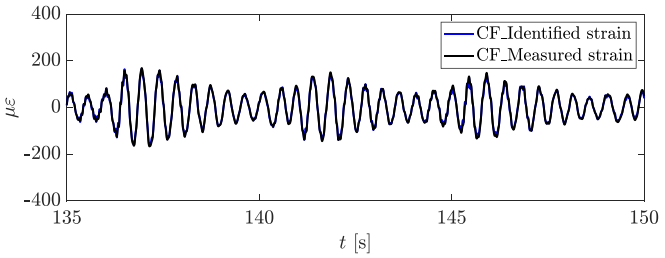

FIG. 5. Comparison between the identified and measured strain in the case $V_r = 8$, KC $= 160$ at FBG-CF3.

For the test pipe model, the modal shapes of the displacement can be treated as the modal shape of the beam pinned at both ends, which can be expressed as

$$\varphi_i(z) = \sin\frac{i\pi z}{L}, \quad i = 1, 2, \ldots. \tag{16}$$

The modal shapes of the curvature $\varphi''(z)$ are also sinusoidal, and the strain can be calculated by

$$\varepsilon(z,t) = -R\sum_{i=1}^{n}\left(\frac{i\pi}{l}\right)^2 p_i(t)\varphi_i(z), \quad z \in [0, L], \tag{17}$$

where $\varepsilon(z,t)$ is the VIV bending strain. Then the modal weight of the displacement $p_i(t)$ can be obtained through Fig. 17, and the VIV displacement in the CF direction can be derived directly using Fig. 13. The derivation of VIV displacement in the IL direction $x(z,t)$ follows similarly. Figure 5 shows the comparison result of the identified and measured microstrain ($\mu\varepsilon$) in the case $V_r = 8$, KC $= 160$ at FBG-CF3. The identified strain is obtained by the second-order difference, and the results show the identified CF strains are in good agreement with the measured strain in the time domain.

C. Time-frequency analysis

To investigate the time-frequency feature of the VIV response under bidirectionally sheared flow, wavelet transformation is used. The continuous wavelet transform equation is expressed as

$$\mathrm{WT}_f(a,\tau) = \langle f(t), \psi_{a,\tau}(t)\rangle = a^{-1/2}\int_{-\infty}^{+\infty} f(t)\psi^*\left(\frac{t-\tau}{a}\right)dt, \tag{18}$$

where WT_f is the wavelet transformation coefficient of the time domain signal $f(t)$, which represents the variation in frequency at that timescale. Parameter a is the scale factor, τ is the shift factor, $\psi(t)$ is the mother wavelet, and the Morlet wavelet is chosen as the mother wavelet. Besides wavelet transform, fast Fourier transform (FFT) is applied for determining the frequency components of the VIV response of the pipe [23–25].

IV. RESULTS AND DISCUSSION

A. VIV responses in the oscillatory sheared flow

Figure 6 shows the VIV response at the case with $V_r = 6$, KC $= 60$ at FBG3-CF with five subfigures: (a) displacement of the edge measured by the encoder during the experiment; (b) theoretical time varying shedding frequency calculated by

$$f_{st} = \frac{\mathrm{St}U_g}{D}, \tag{19}$$

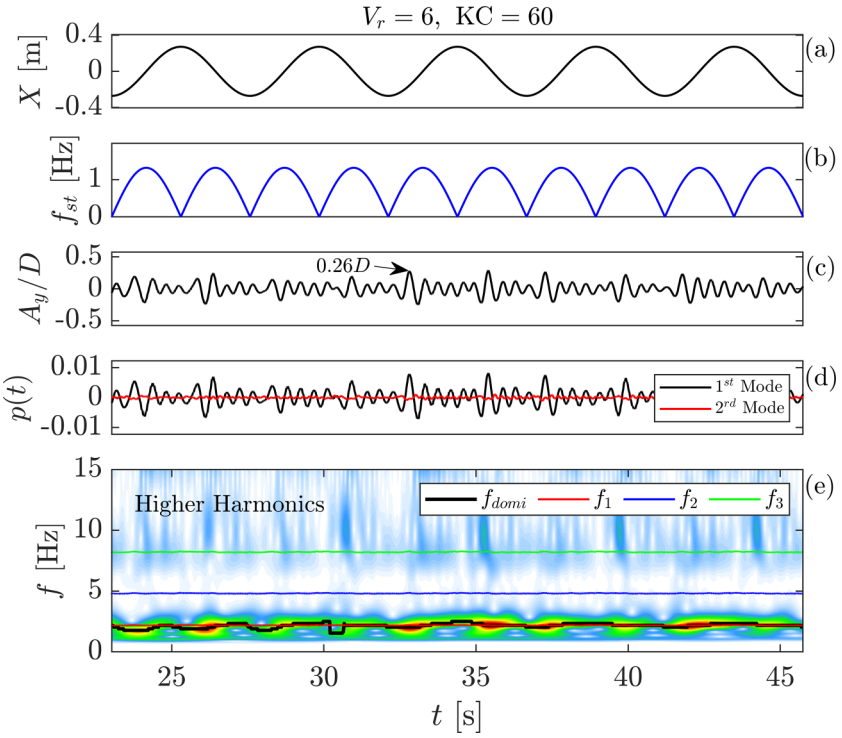

FIG. 6. VIV response in case $V_r = 6$, KC $= 60$ at FBG-CF3. From top to bottom: (a) displacement of the edge; (b) theoretical time varying shedding frequency; (c) normalized time-varying VIV displacement; (d) modal weight of the first and second mode (black line: the first modal weight, red line: the second modal weight); and (e) time-varying response frequency by wavelet analysis (black line: dominant frequency by wavelet analysis, red line: instantaneous natural frequency of the first mode, blue line: second mode, green line: second mode).

where the Strouhal number St $= 0.20$, U_g is the calculated relative flow velocity of the gauge point and D is the diameter of the tested pipe; (c) normalized time-varying VIV displacement in the CF direction by modal analysis; (d) modal weight of the first and second modes calculated by modal analysis; and (e) time-varying VIV frequency by wavelet analysis and instantaneous natural frequency in the first three modes based on measured tension calculated by Fig. 1.

Figure 6 shows that the VIV response in small V_r and KC is relatively stable with a maximum response amplitude of $0.26D$. The VIV response is dominated by the first mode with higher harmonics. Figure 7 displays the VIV response under the case with $V_r = 8,\ \mathrm{KC} = 160$, and it can be seen that an obvious modulated VIV response occurs with a maximum response amplitude of $0.47D$. The modulated VIV response is divided into three regions: building up region, lock-in region, and dying out region. There also exists an obvious higher harmonic in this case. Compared with the low V_r and KC cases, the modulated vibration is more significant, and the vibration is dominated by the first order in the present experiment. The γ parameter defined as

$$\gamma = \frac{\partial U}{\partial t}\frac{D}{U_{\max}^2} \tag{20}$$

is proposed to evaluate the rate of flow velocity change, where U is the time-varying velocity, D is the diameter and $U_{\max}$ is the maximum velocity. Figure 8 displays the forced motion and corresponding γ in the case $V_r = 60$ and KC $= 120$ with the same $V_r = 8$. The black line (small KC) represents a low motion amplitude but a high γ, which means the flow velocity changes more

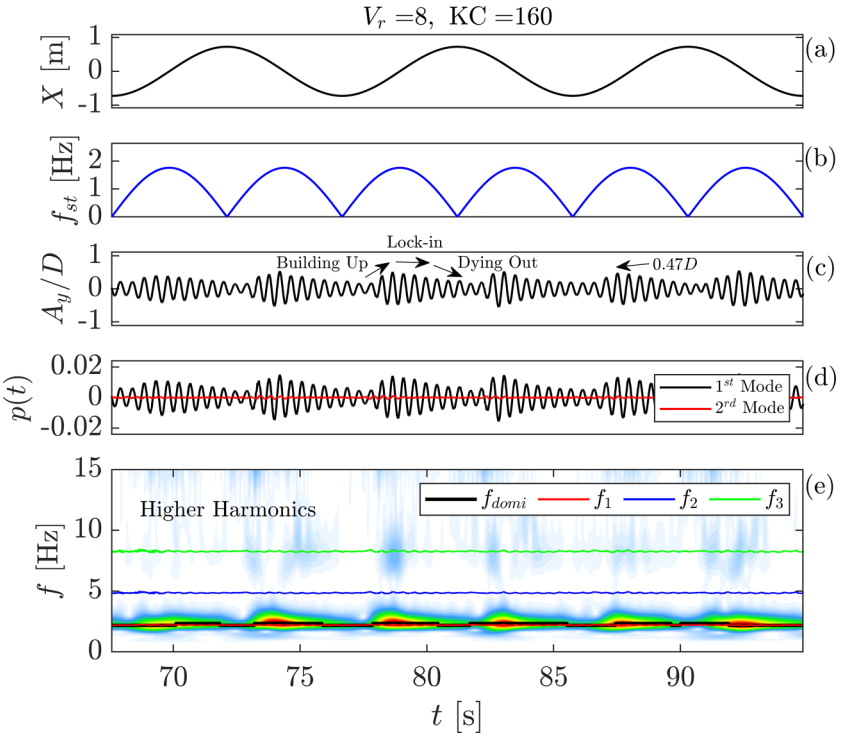

FIG. 7. VIV response in case $V_r = 8$, KC $= 160$ at FBG-CF3. From top to bottom: (a) displacement of the edge; (b) theoretical time varying shedding frequency; (c) normalized time-varying VIV displacement; (d) modal weight of the first and second mode; and (e) time-varying response frequency by wavelet analysis.

rapidly. Therefore, the velocity changes rapidly in small V_r and KC cases where the flexible pipe cannot react quickly enough to build up the VIV response, which results in a stable response. More research on the mechanism of γ will be conducted in the future.

The time-varying response results of the oscillatory sheared flow-induced VIVs are nearly the same as those of linearly oscillatory flow [17].

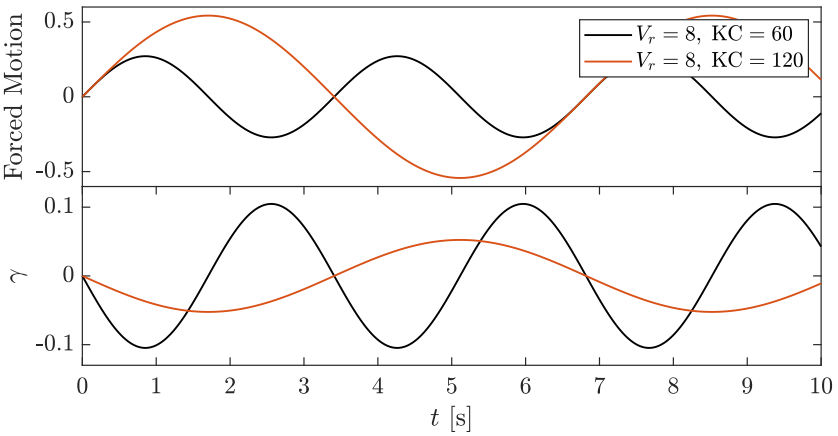

FIG. 8. Forced motion and corresponding γ in different KC case (same V_r).

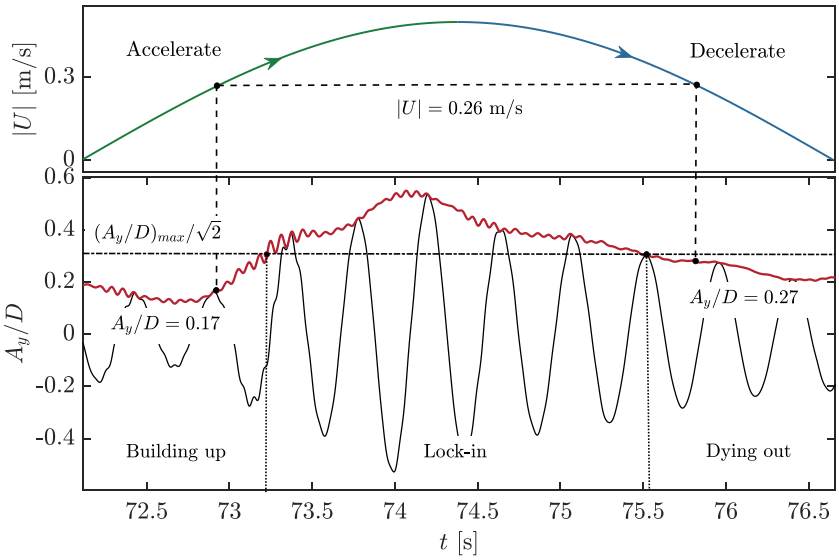

FIG. 9. VIV response in case $V_r = 8$, KC = 160 at FBG-CF3 in the half-period. From top to bottom: absolute value of relative flow velocity at the gauge point of the half period; normalized time-varying VIV displacement. Green line: acceleration region, blue line: deceleration region, black line: time-varying VIV response, red line: instantaneous displacement envelope by a Hilbert transform, dotted line: discriminate line for three regions with the value of $(A_y/D)_{\max}/\sqrt{2}$.

B. Hysteresis

Hysteresis is a phenomenon discovered in bluff cylinder VIV systems in which the VIV response is inconsistent in the acceleration and deceleration regions [26]. Figure 9 displays the time-varying response in the case with $V_r = 8$ and KC = 160 at the FBG-CF3 gauge point. The green and blue lines represent the acceleration and deceleration regions in the half-motion period, respectively. The black and red lines represent the normalized time-varying VIV displacement and instantaneous displacement envelope, respectively. The distribution of the VIV displacements in the acceleration and deceleration regions is not entirely symmetrical. When $|U| = 0.26$ m/s, A_y/D is 0.17 in the acceleration region and 0.27 in the deceleration region. The absolute value of the gradient of the response amplitude increase in the acceleration region is larger than that in the deceleration region. Moreover, the dotted line with a value of $(A_y/D)_{\max}/\sqrt{2}$ separates the response into three regions called the building up, lock-in, and dying out regions to describe the developing process.

Figure 10 further demonstrates the response amplitude in the acceleration and deceleration regions with the same effective reduced velocity V_{re} defined as $|U|/f_{cn1}D$. $|U|$ is the instantaneous effective flow velocity, as Fig. 9 shows. The black and red lines represent the response amplitude in the acceleration and deceleration regions, respectively. The arrows depict the V_{r_e} variation in half a cycle. There exists a difference in the response amplitude in the acceleration and deceleration regions. The response in the deceleration is larger than that in the acceleration region at low V_{r_e}. Combining our previous experimental results on VIVs under uniform oscillatory flow, the hysteresis phenomenon in oscillatory flow-induced VIVs can be defined as *smaller gradients in the VIV response in the deceleration region compared to the acceleration region.* Hydrodynamic analysis shows that the flexible pipe extracts more energy from the fluid to support the vibration which resulted in a higher gradient as the Appendix shows.

C. Strouhal number

Figure 11 displays the response frequencies at different locations of different cases. The displacement of the edge and time-varying response frequency at $Z = L/6$, $L/2$, and $5L/6$ are shown from

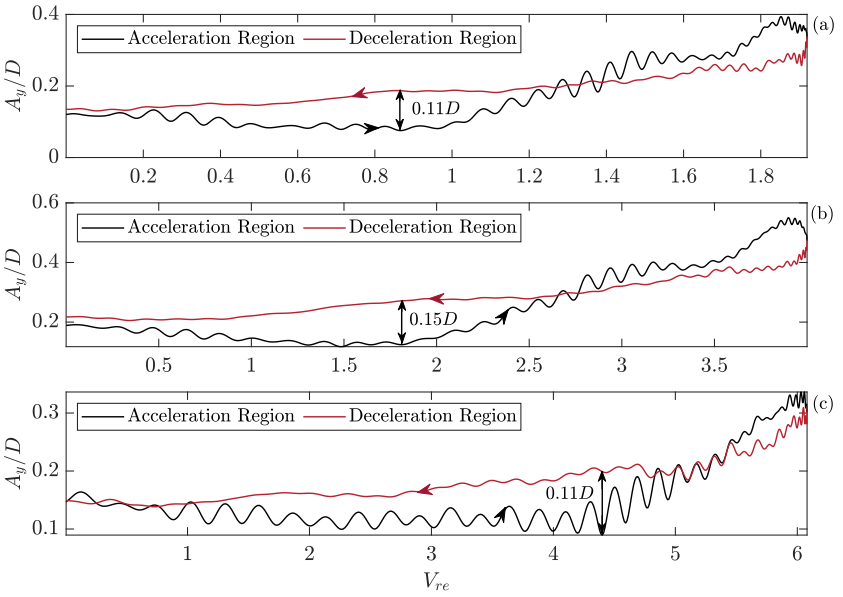

FIG. 10. Hysteresis process in case $V_r = 8$, KC $= 160$ at different gauge points. Red line: VIV response in the deceleration region; black line: VIV response in the deceleration region. (a) Hysteresis process in FBG-CF1; (b) hysteresis process in FBG-CF3; (c) hysteresis process in FBG-CF5.

top to bottom. The black line on the right is the corresponding FFT result based on the time-domain signal. The results show that the dominant frequencies are consistent in the time domain and there exist more higher harmonic signals in the small V_r and KC case. The results are similar with Fig. 6 and Fig. 7. The FFT results of the small V_r and KC case present more frequency components than the large V_r and KC case, and the frequency components are basically the same along the cylinder.

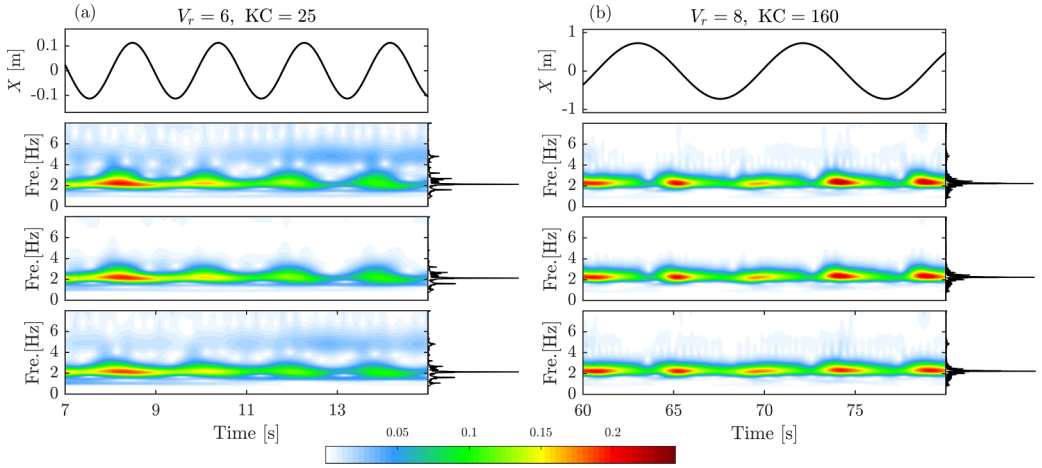

FIG. 11. Response frequencies at different locations of different cases. From top to bottom: displacement of the edge; time-varying response frequency at $Z = L/6$, $L/2$, and $5L/6$, respectively. Black line on the right represents the corresponding FFT results. (a) $V_r = 6$, KC $= 25$ case; (b) $V_r = 8$, KC $= 160$ case.

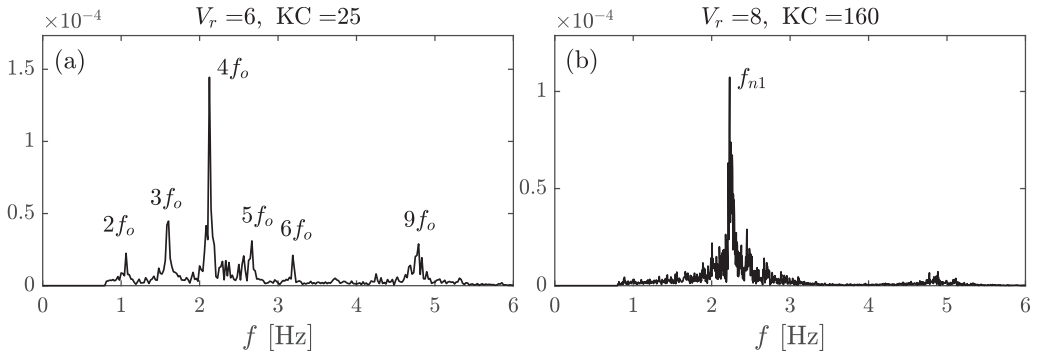

FIG. 12. General frequency spectrum of case (a) $V_r = 6$, ; = 25 (b) $V_r = 8$, KC = 160.

The dominant response frequency is defined in the present study as

$$f_{\text{domi}} = \arg\max_f \mathcal{F}(f) = \arg\max_f \sum_{i=1}^{n} \hat{\mathcal{F}}_i(f), \tag{21}$$

where f_{domi} is the dominant response frequency, $\mathcal{F}(f)$ is the general frequency spectrum defined as the sum of the power spectral density of the measured signal at the ith strain gauge point $\hat{\mathcal{F}}_i(f)$, and n is the number of strain gauges, which is five for the CF direction in the present study. It should be noted that the FFT method is not the optimal approach to determine the dominant frequency for time-varying signal. The FFT and wavelet transform results are similar and basically the same along the pipe, therefore FFT is employed to obtain the dominant response frequency.

Figure 12 represents the general frequency spectrum $\mathcal{F}(f)$ in the cases with $V_r = 6$, KC = 25 and $V_r = 8$, KC = 160. In the low KC cases, the dominant frequency always locks in the multi-frequency response close to the natural frequency. The dominant frequency in the case of KC = 25 is 2.13 Hz ($4f_o$). The higher harmonic response, which includes the second, third, fifth, sixth, and ninth harmonics, is also involved in the VIV response. For cases with large KC, broadband spectra with a dominant frequency close to the natural frequency exist.

The number of vortex shedding (frequency ratio) N is defined as

$$N = \frac{f_{\text{domi}}}{f_o}, \tag{22}$$

where f_o is the frequency of oscillation. Then we have the Strouhal number St expressed as

$$\text{St} = \frac{N}{\text{KC}} = \frac{f_{\text{domi}} D}{U_m}. \tag{23}$$

St reflects the VIV excitation effect of the flow field. A larger St indicates that the flow field can potentially excite a higher VIV response frequency. St of the VIV response under uniform flow is chosen as 0.18. It should be noted that St is used for the vortex shedding frequency prediction first, and it is used for the description of slender structure vibration frequency in steady flow later [22] (also nondimensional frequency [23]). In the present study, the background flow velocity varies with time, and the St is not stable, leading to an unstable response frequency [27,28]. St is estimated by the dominant frequency obtained by FFT, and the applicability of proposed St for VIV prediction in unsteady flow will be investigated further.

Figure 13 displays the number of vortex shedding N vs KC in different cases. The black circles represent the result obtained from the experiment, the black line represents the fitted result based on the scatter experimental results, and the blue line represents the result with St = 0.13, which is proposed for the linearly sheared flow-induced VIV frequency prediction [29]. St is approximately

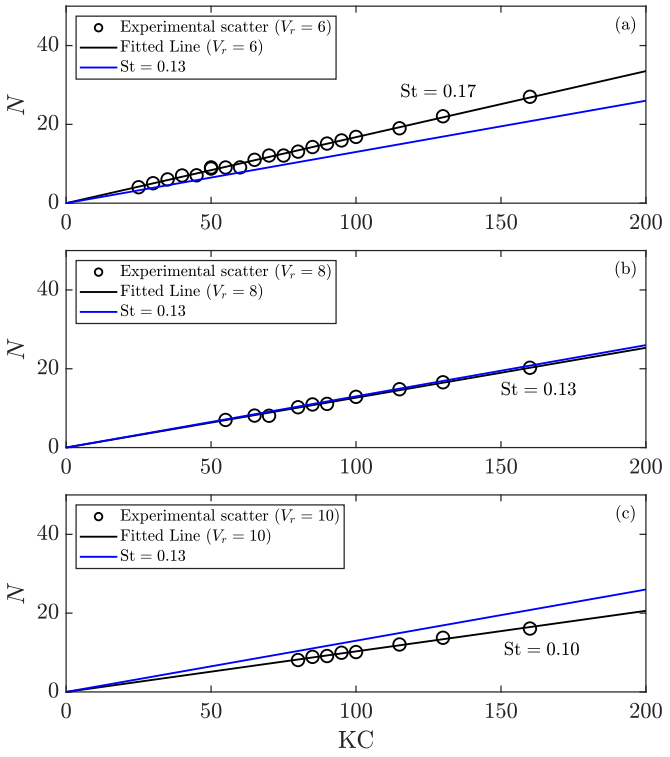

FIG. 13. Number of vortex shedding vs KC number for different cases: (a) $V_r = 6$, (b) $V_r = 8$, and (c) $V_r = 10$. Black circle: results of the different cases obtained from the experiment; black line: fitted line based on the experimental data. Blue line: curve with the slope (St) of 0.13.

0.17 in the case with $V_r = 6$ and 0.13 in the case with $V_r = 8$ and 0.10 and in the case with $V_r = 10$. For the case of $V_r = 8$, St is basically the same with the linearly sheared flow case, St decreases with the V_r increased.

Figure 14 represents the St result with different V_r. The results show that St basically decreases with an increasing V_r in the present study. It should be noted that in the oscillatory sheared flow test represented in the present study, as well as the previously investigated oscillatory uniform flow test, the VIV response is dominated by the first order in most cases. This Strouhal number law reported in Fig. 14 is significantly influenced by the first-order dominant VIV. Future work will cover the experimental study of the oscillatory flow-induced high-mode VIV.

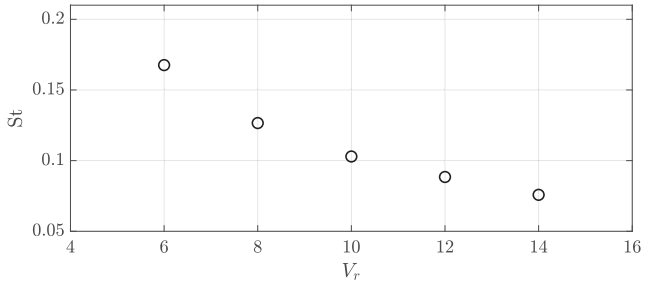

FIG. 14. Summarized relationship of the fitted St results with different V_r.

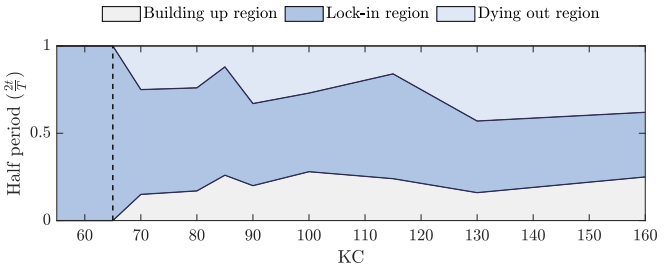

FIG. 15. Time interval distribution of the VIV developing process with $V_r = 8$. Gray area: building up region, deep blue: lock-in region, light blue: dying out region.

D. VIV developing process in oscillatory sheared flow

As Fig. 7 states, there exist three regions in the developing process in oscillatory sheared flow. We use the value of $(A_y/D)_{\max}/\sqrt{2}$ to determine the three regions quantitatively. Figure 15 and Fig. 16 display the time interval distribution of the VIV developing process in the cases with $V_r = 8$ and $V_r = 10$, respectively.

There exists a critical KC. The response with the KC smaller than the critical KC is steady, which is similar to the behavior of steady flow-induced VIVs. When KC is larger than the critical KC, a modulation response occurs with three developing regions. The critical KC in the case with $V_r = 8$, 10 is 65 and 85. The critical KC increases as the reduced velocity increases. With a further increase in KC larger than 100, the VIV development process stabilizes with an approximately 50% lock-in region. The critical KC is related to the γ parameter; further mechanism studies about critical KC and γ will be carried out in the future.

V. SUMMARY

In the present study, we conducted an experiment with a flexible pipe that is 28.41 mm in diameter and 3.88 m in length. One end of the test pipe is fixed, and one end is forced to harmonically oscillate to simulate oscillatory sheared flow with various combinations of amplitudes and periods, with KC numbers from 25 to 160, and with five kinds of reduced velocities V_r from 6 to 14.

There exists an obvious modulated response in oscillatory sheared flow-induced VIV with the building up region, lock-in region, and dying out region at high KC. As KC increases, the lock-in region reaches a constant time interval distribution of nearly 50%. Additionally, the hysteresis phenomenon occurs in oscillatory sheared flow-induced VIV with a relative higher response amplitude and smaller gradient in the deceleration region.

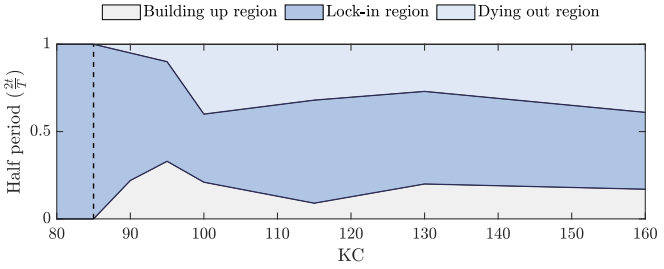

FIG. 16. Time interval distribution of the VIV developing process with $V_r = 10$. Gray area: building up region, deep blue: lock-in region, light blue: dying out region.

The response frequency represents multifrequency with forced vibration frequency harmonics at low KC cases and broadband response at large KC cases. The Strouhal number in oscillatory sheared flow-induced VIV is relatively smaller than that in oscillatory uniform flow and decreases as the reduced velocity increases.

The St and critical KC proposed in the present study will be the input for the VIV prediction method for engineering applicant, and corresponding research will be conducted soon.

ACKNOWLEDGMENTS

The authors gratefully acknowledge the financial support from the National Natural Science Foundation of China under Grants No. 52001208 and No. 52088102, the Fundamental Research Funds for the Central Universities, National Key Research and Development Program of China under Grant No. 2023YFC2811600, the Shanghai Science and Technology Program under Grants No. 21ZR1434500 and No. 22ZR1434100, the State Key Laboratory of Ocean Engineering (Shanghai Jiao Tong University) under Grant No. GKZD010081, the Shenlan Project under Grant No. SL2021MS018, and the Young Elite Scientists Sponsorship Program under Grant No. 2020QNRC001. The authors would also like to express gratitude to DNV for preparing the experiment.

APPENDIX: MECHANISM OF HYSTERESIS

In this Appendix, the mechanism of hysteresis is investigated briefly by the VIV force identification theory and the forgetting factor least squares algorithm (FFLS). The VIV force of the pipe can be identified by Euler-Bernoulli beam theory as

$$\mathrm{EI}\frac{\partial^4 y(z,t)}{\partial z^4} - \frac{\partial}{\partial z}\left[T(t)\frac{\partial y(z,t)}{\partial z}\right] + c\frac{\partial y(z,t)}{\partial t} + \bar{m}\frac{\partial^2 y(z,t)}{\partial t^2} = F_{\mathrm{total}}(z,t), \tag{A1}$$

where EI is the bending stiffness, $\bar{m}$ is the mass per unit length in air, $T(t)$ is the time-varying tension, $c = 2\bar{m}\omega\zeta$ is structural damping, ω is the dominant circular frequency, and ζ is damping ratio (see Table I). The VIV force can be decomposed as excitation force F_e in phase with velocity and added mass force F_m in phase with acceleration as

$$F_{\mathrm{total}}(t) = \underbrace{\frac{\dot{y}(t)}{2|\dot{y}(t)|}\rho D V(t)^2 C_e(t)}_{F_e} \underbrace{-\frac{\pi D^2}{4}\rho C_m(t)\ddot{y}(t)}_{F_m}, \tag{A2}$$

where C_e is the excitation coefficient, C_m is the added mass coefficient, V is the flow velocity at z location, and the diagram of the force decomposition method is shown in Fig. 17.

Then the FFLS algorithm is applied for the identification of the time-varying VIV force coefficients, and Eq. (A2) can be rewritten as [30,31]

$$\begin{aligned}
\mathbf{F}_s^* &= \mathbf{H}_s^* \boldsymbol{\theta}_s, \\
\mathbf{F}_s^* &= \left[\beta^{s-1}F_{\mathrm{total}}(t_1), \beta^{s-2}F_{\mathrm{total}}^*(t_2), \beta^{s-3}F_{\mathrm{total}}(t_3), \ldots, \beta^0 F_{\mathrm{total}}(t_s)\right]^T, \\
\mathbf{H}_s^* &= [\beta^{s-1}\boldsymbol{h}(1), \beta^{s-2}\boldsymbol{h}(2), \beta^{s-3}\boldsymbol{h}(3), \ldots, \beta^0\boldsymbol{h}(s)]^T \\
&= \begin{bmatrix} \dot{y}(t_1), \dot{y}(t_2), \dot{y}(t_3), \ldots, \dot{y}(t_s) \\ \ddot{y}(t_1), \ddot{y}(t_2), \ddot{y}(t_3), \ldots, \ddot{y}(t_s) \end{bmatrix}^T, \\
\boldsymbol{\theta}(\mathrm{s}) &= \begin{bmatrix} \frac{\rho D V(t)^2}{2|\dot{y}(t)|}C_e(t_s) \\ -\frac{\rho\pi D^2}{4}C_m(t_s) \end{bmatrix}, \\
s &\in \mathbb{N}^+,
\end{aligned} \tag{A3}$$

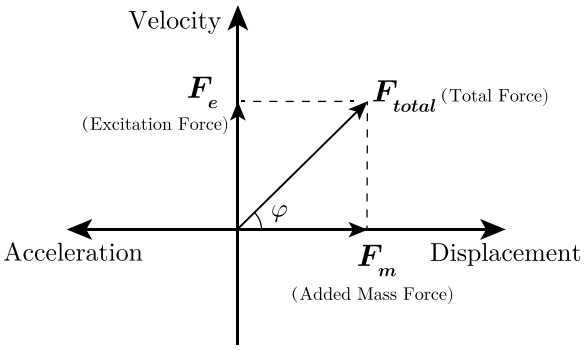

FIG. 17. Diagram of the force decomposition method. φ is the phase difference between the total lift force and the displacement [30].

where $\beta \in (0, 1]$ represents the forgetting factor, $\beta = 1.00$ in the least squares algorithm. The parameters to be identified need to minimize the sum of the squared errors between $\mathbf{H}_s^*\boldsymbol{\theta}_s$ and $\mathbf{F}_{\text{total}}^*$ as

$$\left.\frac{\partial J(\boldsymbol{\theta})}{\partial \boldsymbol{\theta}}\right|_{\widehat{\boldsymbol{\theta}}_s} = \left.\frac{\partial}{\partial \boldsymbol{\theta}}(\mathbf{F}_s^* - \mathbf{H}_s^*\boldsymbol{\theta}_s)^T(\mathbf{F}_s^* - \mathbf{H}_s^*\boldsymbol{\theta}_s)\right|_{\widehat{\boldsymbol{\theta}}_s} = \mathbf{0}, \tag{A4}$$

and then we can have

$$\widehat{\boldsymbol{\theta}}_s = \left(\mathbf{H}_s^{*T}\mathbf{H}_s^*\right)^{-1}\mathbf{H}_s^{*T}\mathbf{F}_s^*. \tag{A5}$$

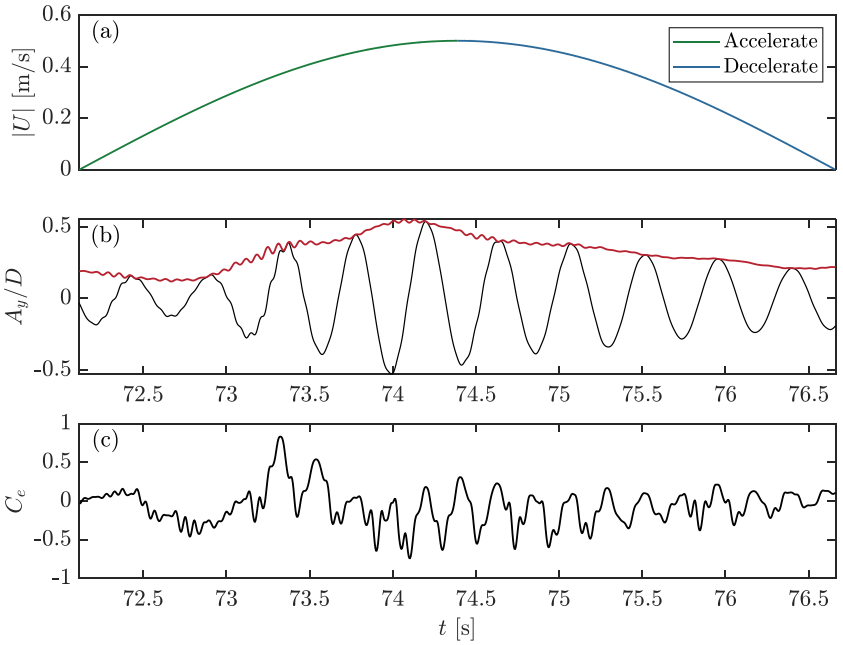

FIG. 18. VIV hydrodynamic of the case $V_r = 8$, KC $= 160$ at the FBG-CF3 point: (a) absolute value of relative flow velocity; (b) VIV displacement; (c) time-varying excitation coefficient C_e at FBG-CF3 point.

Substituting Eq. (A3) into Eq. (A5), we can finally obtain

$$\begin{aligned}\widehat{\boldsymbol{\theta}}_s &= \left[\sum_{i=1}^{s} \beta^{2(s-i)} \boldsymbol{h}(i)\boldsymbol{h}^T(i)\right]^{-1}\left[\sum_{i=1}^{s} \beta^{2(s-i)} \boldsymbol{h}(i)F_{\text{total}}(i)\right] \\ &= \left[\sum_{i=1}^{s} \mu^{(s-i)} \boldsymbol{h}(i)\boldsymbol{h}^T(i)\right]^{-1}\left[\sum_{i=1}^{s} \mu^{(s-i)} \boldsymbol{h}(i)F_{\text{total}}(i)\right] \\ &= \left(\boldsymbol{H}_s^T \boldsymbol{\Lambda}_s \boldsymbol{H}_s\right)^{-1} \boldsymbol{H}_s{}^T \boldsymbol{\Lambda}_s \boldsymbol{F}_s,\end{aligned} \tag{A6}$$

where $\mu = \beta^2$, $\mu \in (0, 1]$, μ is called the forgetting factor, and Λ_s is the weighted matrix, which is a diagonal matrix $\Lambda_s = \text{diag}(\mu^{s-1}, \mu^{s-2}, \ldots, \mu, 1)$. The essence of this method is to give different weights to the data depending on the moment of data.

Excitation coefficient C_e represents the energy transfer between fluid and structure. A positive C_e means that energy transfers from fluid to structure. Figure 18 displays the time-varying response and excitation coefficient of a half circle. In the acceleration region, there exists a positive peak value of excitation coefficient C_e. C_e exhibits periodic variations but does not show distinct positive peaks in the deceleration region. This implies that during the acceleration region, compared to the deceleration phase, the flexible pipe extracts more energy from the fluid to support the vibration, which resulted in a higher gradient. More detailed fluid-structure interaction mechanism analysis will be conducted based on further CFD research.

[1] M. Tognarelli, S. Slocum, W. Frank, and R. Campbell, VIV response of a long flexible cylinder in uniform and linearly sheared currents, in *Paper Presented at the Offshore Technology Conference, Houston, Texas, May 2004*, OTC Offshore Technology Conference (OnePetro, 2004), paper OTC-16338-MS.

[2] C. H. Williamson and R. Govardhan, Vortex-induced vibrations, Annu. Rev. Fluid Mech. **36**, 413 (2004).

[3] T. Sarpkaya, A critical review of the intrinsic nature of vortex-induced vibrations, J. Fluids Struct. **19**, 389 (2004).

[4] C. Williamson and R. Govardhan, A brief review of recent results in vortex-induced vibrations, J. Wind Eng. Ind. Aerodyn. **96**, 713 (2008).

[5] K.-S. Hong and U. H. Shah, Vortex-induced vibrations and control of marine risers: A review, Ocean Eng. **152**, 300 (2018).

[6] J. Duan, J. Zhou, Y. You, and X. Wang, Effect of internal flow on vortex-induced vibration dynamics of a flexible mining riser in external shear current, Marine Struct. **80**, 103094 (2021).

[7] P. R. Boersma, J. P. Rothstein, and Y. Modarres-Sadeghi, Experimental investigation of vortex-induced vibrations of a flexibly mounted cylinder in a shear-thinning fluid, Phys. Rev. Fluids **8**, 044703 (2023).

[8] A. Trim, H. Braaten, H. Lie, and M. Tognarelli, Experimental investigation of vortex-induced vibration of long marine risers, J. Fluids Struct. **21**, 335 (2005).

[9] L. Song, S. Fu, S. Dai, M. Zhang, and Y. Chen, Distribution of drag force coefficient along a flexible riser undergoing VIV in sheared flow, Ocean Eng. **126**, 1 (2016).

[10] J. Chaplin, P. Bearman, F. H. Huarte, and R. Pattenden, Laboratory measurements of vortex-induced vibrations of a vertical tension riser in a stepped current, J. Fluids Struct. **21**, 3 (2005).

[11] Q. Han, Y. Ma, W. Xu, Y. Lu, and A. Cheng, Dynamic characteristics of an inclined flexible cylinder undergoing vortex-induced vibrations, J. Sound Vib. **394**, 306 (2017).

[12] K. Vikestad, C. M. Larsen, and J. K. Vandiver, Norwegian deepwater program: Damping of vortex-induced vibrations, in *Paper Presented at the Offshore Technology Conference, Houston, Texas, May 2000*, OTC Offshore Technology Conference (OnePetro, 2000), paper OTC-11998-MS.

[13] A Report From the Drilling Riser VIV and Wellhead Fatigue JIP Full-Scale Drilling Riser VIV Measurements and Comparisons With Predictions, https://asmedigitalcollection.asme.org/OMAE/proceedings-abstract/OMAE2023/86892/1167268.

[14] D. Yin, J. Wu, H. Lie, E. Passano, S. Sævik, G. Grytoyr, M. A. Tognarelli, T. Andersen, R. Igland, D. Karunakaran, and C. Gaskill, Vortex-induced vibrations of a top-tensioned riser in combined currents and waves, in *Proceedings of the ASME 2022 41st International Conference on Ocean, Offshore and Arctic Engineering, Hamburg, Germany, June 5–10, 2022*, Volume 7: CFD and FSI (ASME, 2022), paper OMAE2022-79033, V007T08A028.

[15] M. Triantafyllou, G. Triantafyllou, Y. Tein, and B. D. Ambrose, Pragmatic riser VIV analysis, in *Paper Presented at the Offshore Technology Conference, Houston, Texas, May 1999*, OTC Offshore Technology Conference (OnePetro, 1999), paper OTC-10931-MS.

[16] J. Wang, S. Fu, R. Baarholm, J. Wu, and C. M. Larsen, Out-of-plane vortex-induced vibration of a steel catenary riser caused by vessel motions, Ocean Eng. **109**, 389 (2015).

[17] J. Wang, S. Fu, R. Baarholm, J. Wu, and C. M. Larsen, Fatigue damage induced by vortex-induced vibrations in oscillatory flow, Marine Struct. **40**, 73 (2015).

[18] S. Fu, J. Wang, R. Baarholm, J. Wu, and C. Larsen, Features of vortex-induced vibration in oscillatory flow, J. Offshore Mech. Arctic Eng. **136**, 011801 (2014).

[19] X. Fu, S. Fu, H. Ren, W. Xie, Y. Xu, M. Zhang, Z. Liu, and S. Meng, Experimental investigation of vortex-induced vibration of a flexible pipe in bidirectionally sheared flow, J. Fluids Struct. **114**, 103722 (2022).

[20] X. Fu, M. Zhang, S. Fu, B. Zhao, H. Ren, and Y. Xu, On the study of vortex-induced vibration of a straked pipe in bidirectionally sheared flow, Ocean Eng. **266**, 112945 (2022).

[21] A. Khalak and C. H. Williamson, Investigation of relative effects of mass and damping in vortex-induced vibration of a circular cylinder, J. Wind Eng. Ind. Aerodyn. **69–71**, 341 (1997).

[22] H. Lie and K. Kaasen, Modal analysis of measurements from a large-scale VIV model test of a riser in linearly sheared flow, J. Fluids Struct. **22**, 557 (2006).

[23] M. J. Thorsen, S. Sævik, and C. M. Larsen, Time domain simulation of vortex-induced vibrations in stationary and oscillating flows, J. Fluids Struct. **61**, 1 (2016).

[24] C. Barbi, D. Favier, C. Maresca, and D. Telionis, Vortex shedding and lock-on of a circular cylinder in oscillatory flow, J. Fluid Mech. **170**, 527 (1986).

[25] P.-A. Opinel and N. Srinil, Application of wake oscillators to two-dimensional vortex-induced vibrations of circular cylinders in oscillatory flows, J. Fluids Struct. **96**, 103040 (2020).

[26] N. a. Jauvtis and C. Williamson, The effect of two degrees of freedom on vortex-induced vibration at low mass and damping, J. Fluid Mech. **509**, 23 (2004).

[27] J. Dahl, F. Hover, M. Triantafyllou, and O. Oakley, Dual resonance in vortex-induced vibrations at subcritical and supercritical Reynolds numbers, J. Fluid Mech. **643**, 395 (2010).

[28] J. Dahl, F. Hover, and M. Triantafyllou, Two-degree-of-freedom vortex-induced vibrations using a force assisted apparatus, J. Fluids Struct. **22**, 807 (2006).

[29] Y. Gao, S. Fu, T. Ren, Y. Xiong, and L. Song, VIV response of a long flexible riser fitted with strakes in uniform and linearly sheared currents, Appl. Ocean Res. **52**, 102 (2015).

[30] X. Fu, S. Fu, M. Zhang, Z. Han, H. Ren, Y. Xu, and B. Zhao, Frequency capture phenomenon in tandem cylinders with different diameters undergoing flow-induced vibration, Phys. Fluids **34**, 085120 (2022).

[31] C. Liu, S. Fu, M. Zhang, and H. Ren, Time-varying hydrodynamics of a flexible riser under multi-frequency vortex-induced vibrations, J. Fluids Struct. **80**, 217 (2018).